Supplemental Online Material for:

Deep mantle plumes and convective upwelling beneath the Pacific Ocean

Nicholas Schmerr
Edward Garnero
Allen McNamara

Supplemental Methods

Here we present a catalog of stacks for each discontinuity (Figs. S1-S2) and explore in more detail several potential sources of error in our upper mantle discontinuity observations. We perform a series of seismic signal processing experiments to demonstrate the effects of frequency content, interfering phases (Figs. S3-S4), standard errors (Figs. S5-S6), and the corrections for upper mantle structure on the resulting discontinuity topography and MTZ thickness.

Signal Processing Tests

We low-pass filter our dataset to investigate the sensitivity of resulting topography to various frequencies. Shorter period data are more sensitive to smaller scale discontinuity structure; a past theoretical investigation of the sensitivity of the SS precursors to topographic structure showed that it is possible to properly retrieve structure from a 30 second dominant period wave interacting with a 50 km depression of ~3000 km in wavelength (Chaljub and Tarantola, 1997). We investigate data down to periods of 10 seconds (though in general the most stable results are found at 15 seconds), implying a sensitivity of SS precursors to structure near 1000 km in wavelength, though this is an approximation at best. To further investigate this parameter, we present results for the discontinuity topography and MTZ thickness for the 25-second low-pass filtered data (Fig. 3, second row). Many of the large-scale features in the image constructed from the 15 sec low-passed data are indeed visible in the images made from the 25 sec low-passed data, such as the thickened transition zone beneath the New Hebrides subduction zone and thinned MTZ beneath Hawaii, but the smaller scale structures are lost (e.g., the province of thinning in the southern Pacific, and the thickening of the MTZ beneath Cascadia). Thus we are resolving smaller-scale feature by utilizing shorter period waves.

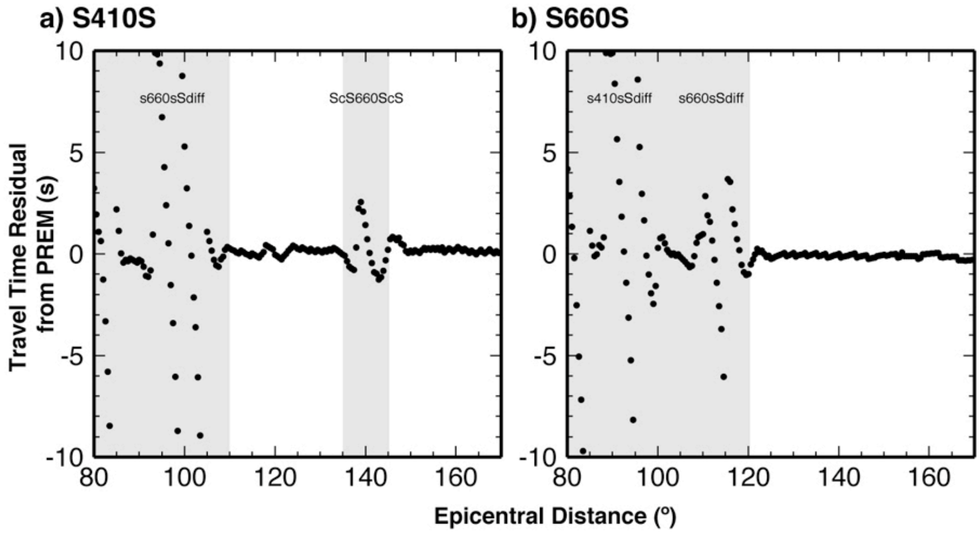

Fig. S3. Synthetic waveform travel times demonstrating the effect of interfering seismic phases on the SS precursors, low-pass filtered at 15 seconds. a) Travel time picks for stacks of the synthetic dataset every 0.5 degrees in epicentral distance for the 410 km discontinuity precursor. b) The same as panel a except for the 660 km discontinuity precursor. Calculation of the travel time residual is described in the text. The gray shading demarks distances that we exclude from our dataset; the corresponding interfering phases are labeled at the top.

If a stack is populated primarily by seismograms from an epicentral distance in which an interfering phase dominates (e.g., consider the S660S precursor in Fig. 2 at 100-110 degrees, which is contaminated by the stronger s660sS_{diff}), the resulting depth measurement will be in error; masking epicentral distance and timing windows with known interference from other phases circumvents this complication. This is revealed in Fig. S3, where precursor travel times are measured at each epicentral distance by determining the maximum amplitude in a ±15 second window around the PREM predicted travel time for PREM synthetic seismograms. We compute a residual time by subtracting the time measured from a synthetic seismogram from the ray theory predicted arrival time. Fig. S3 visibly demonstrates that the effect of travel time contamination from other phases: the travel times of SS precursors are perturbed by 1-4 seconds (and greater), resulting in erroneous estimations of discontinuity topography at these distances. Therefore, we exclude seismograms from our stacks falling within distances (gray shading) that are perturbed by greater than 3 seconds from the expected travel time. Other techniques, such as least squares Radon transform, have also achieved success in reducing such effects (An, et al., 2007).

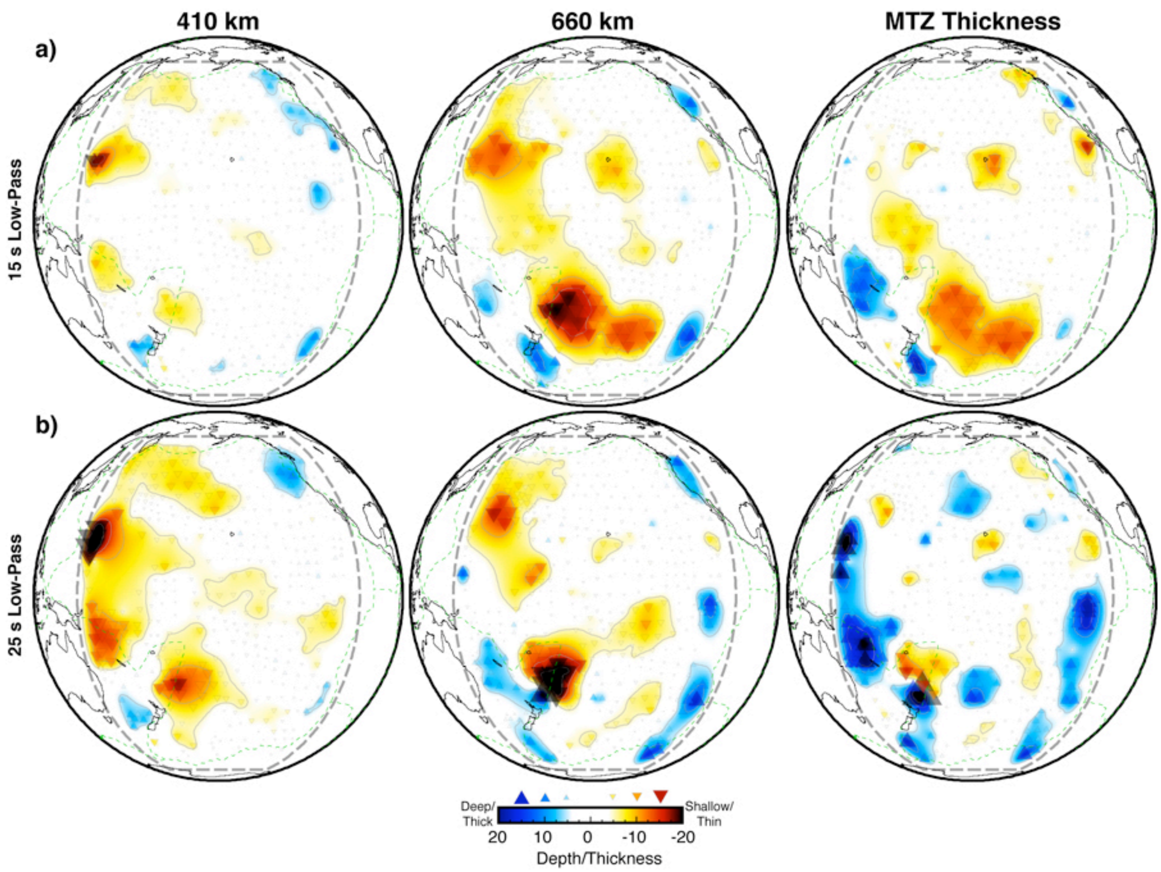

Fig. S4. The effect of interfering seismic phases on the retrieved topography and transition zone thickness. All data from epicentral distance ranges 110-165° are used to construct the stacks in this experiment, allowing the incorporation of non-SS precursor seismic energy. The details are the same as in Fig. 3. a) Data low-pass filtered with a corner at 15 seconds. b) Data low-pass filtered with a corner at 25 seconds.

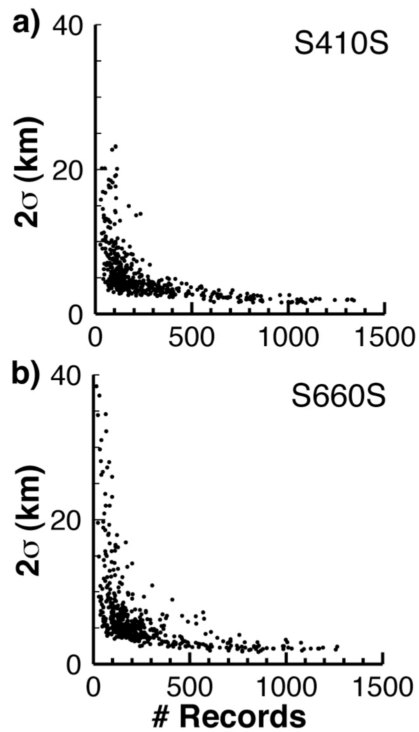

Fig. S5. The standard deviation (2σ) calculated for each stack histogram for a) the 410 km and b) 660 km precursor. The spread of values in each histogram is partially a function of the number of records in a stack, as is shown here for the 15 second low-pass filtered data.

We further quantify the effects of masking data within epicentral distance windows containing interfering energy; we produced stacks without our epicentral distance exclusion criterion (Fig. S4). For data low-pass filtered at 15 seconds, the differences between the topography/thickness maps here and those presented in Fig. 3 are subtle, and mostly confined to the bins with the lowest number of records. For data low-pass filtered at 25 seconds, the effects are profound, with the resulting topography/thickness maps changing significantly compared to those presented in Fig. 3. The long-period result is more susceptible to the effects of interfering phases from the nature of the low-pass filter; peaks from two adjoining phases will be smoothed, producing an averaging of their respective travel times. Distance exclusion remedies this problem and produces more accurate and stable maps of discontinuity structure across various frequencies. The distance exclusion algorithm, along with using more and shorter period data than past work are the principle reasons our results differ from past work.

Stacking of data requires the use of many hundreds of seismograms to produce coherent results and it is necessary to define the criteria that classify a stack as 'robust.' We chose 150 records as a cut-off point for defining well-resolved stacks in our study, as these stacks always possess amplitudes above the 95% confidence interval. Stacks falling below 150 records were required to have a bootstrap standard deviation of less than 10 km (Fig. S5), and stacked amplitudes must fall above the 95% confidence interval to be included in our analysis. Based upon these criteria, we classify 420 out of the 484 stacks in our study region as robust; these stacks are used to construct the topographic and thickness maps in Fig 3.

The stacks possessing large histogram standard deviations are generally associated with regions possessing a relatively low number of records, often located at the edges of the Pacific study region (Fig. S6). An exception to this is the stacks located to the east of the Tonga subduction zone; the large standard deviations seen here originate from a broadened 660 stacked waveform, though the corresponding 410 pulse is relatively sharp with a low standard deviation. Other factors include the noise in the records and the complexity of precursor travel times from Earth structure. Larger numbers of records in a stack tend to average out any major deviations from the mean, resulting in much lower standard deviations.

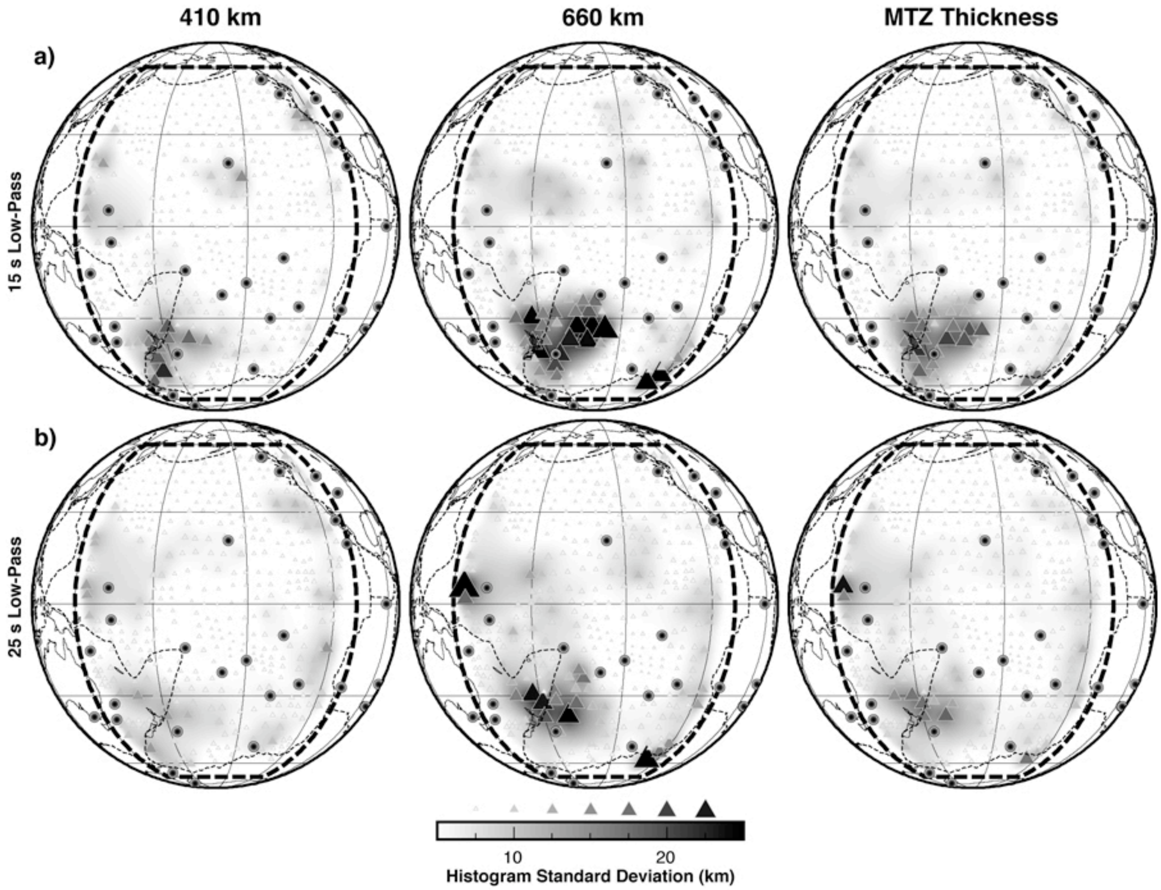

Fig. S6. The standard deviation (2σ) measured from each stack histogram for the discontinuities and MTZ thickness. Triangles are scaled to the standard deviation of each stack and plotted at the average location of bouncepoints within each bin. Also shown is the extent of our data coverage (thick dotted line), plate boundaries (thin dotted line), and hotspots (black dots).

However, in some cases, even well populated stacks show a large spread of estimated discontinuity depths in the bootstrap resamplings. In our Pacific study region, well-populated bins with high standard deviations correspond to stacks located near regions of suspected thermal or chemical heterogeneity, such as subduction zones and hotspots (Fig. S6). Beneath South America, large histogram variations associated with well-populated stacks were shown to be consistent with the presence of multiple discontinuities, or very short-scale, high-relief topography (Schmerr and Garnero, 2007). The region with the highest standard deviation of discontinuity depth estimates occurs in the southwest of our study region, in the southwest portion of the broad 660 km discontinuity upwarping. Close to the Tonga subduction zone there is the possibility that unaccounted for upper mantle heterogeneity contributes to this scatter. However, a large portion of the 660 upwarping is where the standard deviation is not large. We interpret the imaging in the region of high deviation to still contain important information, owing to the fact that the mean discontinuity value is similar result to the bins in the west and east that have higher record numbers, but acknowledge the greater uncertainty. We note that the potential discontinuity perturbation from mis-mapped Tonga slab structure is at a much smaller scale than the overall 660 km discontinuity upwarping, and hence does not alter the conclusions relating to the large-scale upwarping.

Corrections for upper mantle structure

Lateral heterogeneity in the upper mantle perturbs the travel time of the reference SS arrivals. If this heterogeneity is not properly accounted for, the SS travel time anomaly can be mistaken for topography on the upper mantle discontinuities (Zhao and Chevrot, 2003). MTZ thickness is largely free from this effect, though, as mentioned earlier, strong heterogeneity in the MTZ can produce travel time anomalies that map onto the depth of the 410 and 660 km discontinuities. The thinnest MTZ anomaly is located near the subducting Tonga slab, which is opposite of what is expected for a cold downwelling slab passing through the MTZ. Both the 410 km and 660 km discontinuity are shallow in this region, even after a correction for upper mantle heterogeneity; the 660 km occurs 15-25 km above the average depth, and the 410 km is 5-10 km shallower (Figs. 3-4). This correlation of the discontinuities is consistent with a SS wave that is experiencing a travel time advance from passing through a region of high velocity in the upper mantle (discussed in the main text).

We also examined the other large anomalies in the Pacific study region for similar travel time effects, including the large province of thinned MTZ to the east of Tonga, and the thinning beneath and to the south-southeast of Hawaii. To remove the observed discontinuity topography in these regions, it is required that there be a strong, high-velocity shear anomaly in the upper mantle, though this would produce a correlation between the depths of the 2 discontinuities (they are weakly anti-correlated). A high velocity anomaly extending across the upper mantle in these regions is unsupported by tomographic studies; S20RTS and other tomography models find strongly lowered shear-wave velocities above our anomalously thin regions. Alternatively, a small-scale, (< 500 km wide) localized low velocity anomaly directly underlying the 660 km discontinuity at the bounce point would delay the S660S arrival, but not the SS or S410S arrivals, resulting in a 660 km incorrectly mapped to a shallower depth. A wider low velocity anomaly would delay both the S410S and S660S arrivals, and produce correlated topography on the discontinuities. We note that S20RTS does exhibit lowered shear velocities extending into the lower mantle beneath Hawaii, however we correct for the path of S660S through this structure, thus presumably minimizing this effect. The province to the east of Tonga extends over a region several thousand kilometers wide and there is no correlation of the 410 km discontinuity topography with that on the 660 km. Thus we conclude that the MTZ beneath these regions is indeed thinned, though we acknowledge uncertainties exist where tomography does not properly resolve mantle heterogeneity.

Supplemental References

An, Y., Gu, Y.J., Sacchi, M.D., 2007. Imaging mantle discontinuities using least squares Radon transform. Journal of Geophysical Research-Solid Earth 112, doi:10.1029/2007JB005009.

Chaljub, E., Tarantola, A., 1997. Sensitivity of SS precursors to topography on the upper-mantle 660-km discontinuity. Geophysical Research Letters 24, 2613-2616.

Schmerr, N., Garnero, E., 2007. Upper mantle discontinuity topography from thermal and chemical heterogeneity. Science 318, 623-626.

Zhao, L., Chevrot, S., 2003. SS-wave sensitivity to upper mantle structure: Implications for the mapping of transition zone discontinuity topographies. Geophysical Research Letters 30, 1590, doi:1510.1029/2003GL017223.

Supplemental Figures

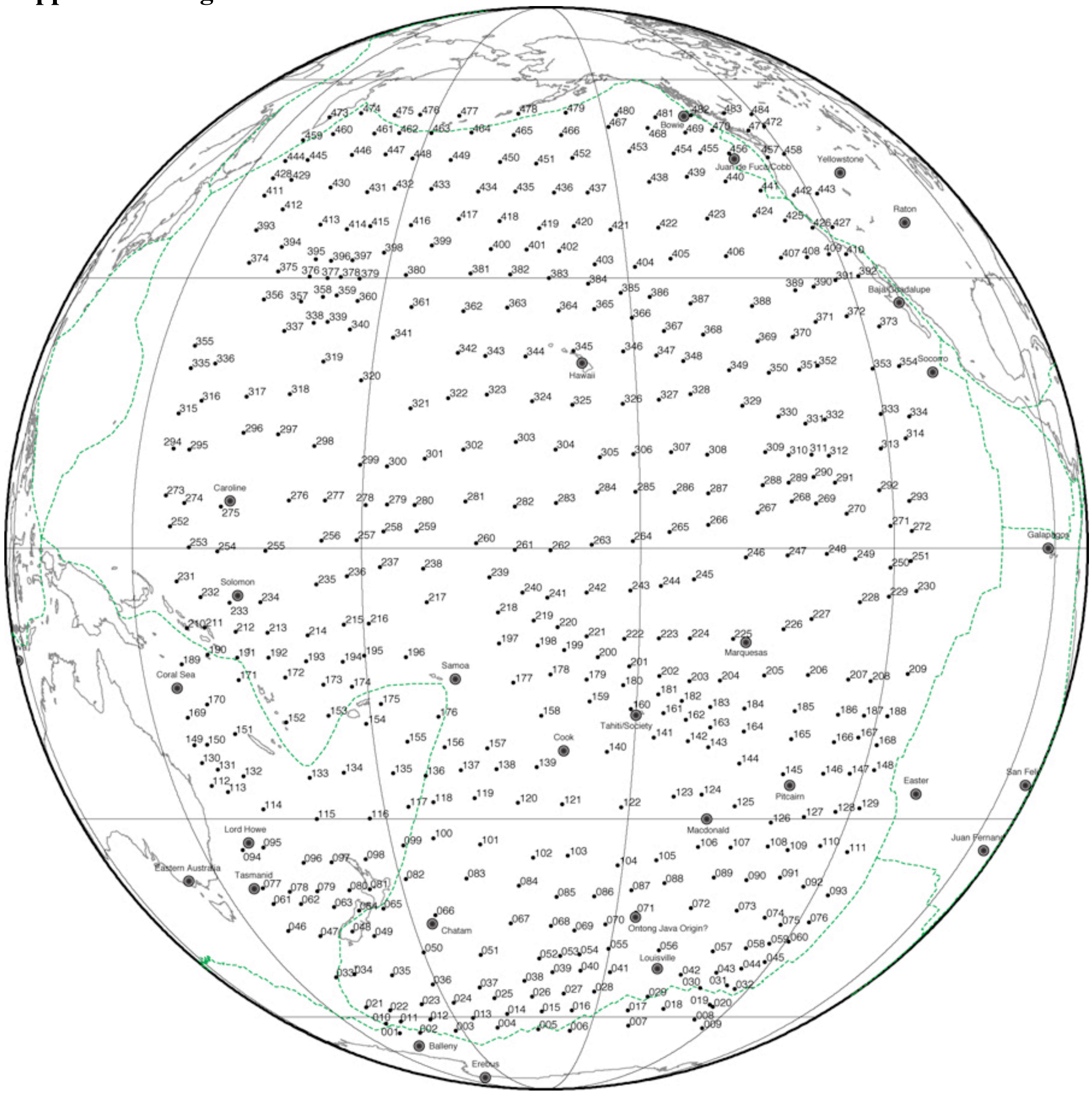

Fig. S1. A map showing the location of each stack; the number corresponds to the bin number given at the upper right of each stack plot in Fig. S2. Hotspots locations used in our study are also identified.

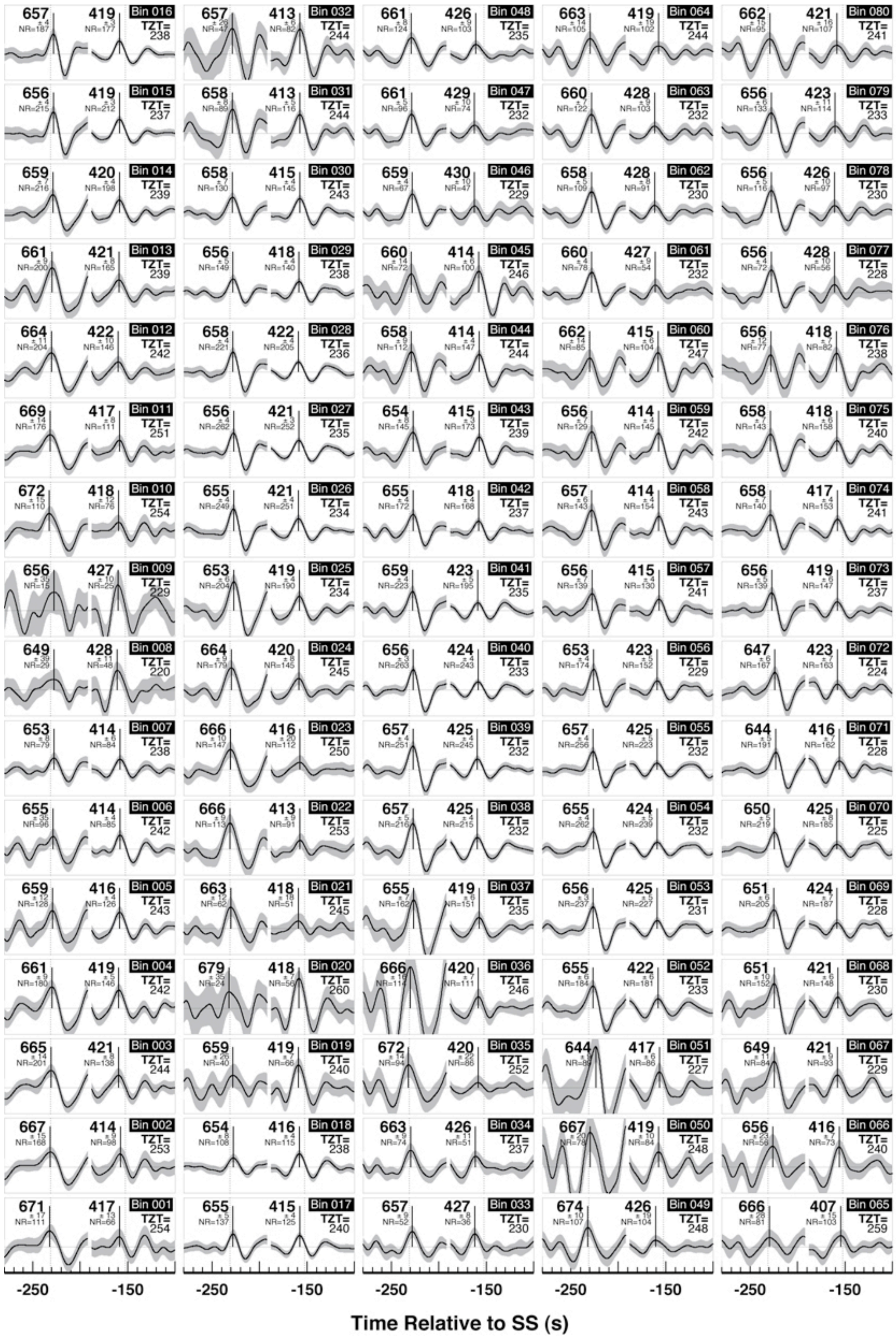

657 419 Bin 016 TZT= 238
656 419 Bin 015 TZT= 237
659 420 Bin 014 TZT= 239
661 421 Bin 013 TZT= 239
664 422 Bin 012 TZT= 242
669 417 Bin 011 TZT= 251
672 418 Bin 010 TZT= 254
656 427 Bin 009 TZT= 229
649 428 Bin 008 TZT= 220
653 414 Bin 007 TZT= 238
655 414 Bin 006 TZT= 242
659 416 Bin 005 TZT= 243
661 419 Bin 004 TZT= 242
665 421 Bin 003 TZT= 244
667 414 Bin 002 TZT= 253
671 417 Bin 001 TZT= 254
657 413 Bin 032 TZT= 244
658 413 Bin 031 TZT= 244
658 415 Bin 030 TZT= 243
656 418 Bin 029 TZT= 238
658 422 Bin 028 TZT= 236
656 421 Bin 027 TZT= 235
655 421 Bin 026 TZT= 234
653 419 Bin 025 TZT= 234
664 420 Bin 024 TZT= 245
666 416 Bin 023 TZT= 250
666 413 Bin 022 TZT= 253
663 418 Bin 021 TZT= 245
679 418 Bin 020 TZT= 260
659 419 Bin 019 TZT= 240
654 416 Bin 018 TZT= 238
655 415 Bin 017 TZT= 240
661 426 Bin 048 TZT= 235
661 429 Bin 047 TZT= 232
659 430 Bin 046 TZT= 229
660 414 Bin 045 TZT= 246
658 414 Bin 044 TZT= 244
654 415 Bin 043 TZT= 239
655 418 Bin 042 TZT= 237
659 423 Bin 041 TZT= 235
656 424 Bin 040 TZT= 233
657 425 Bin 039 TZT= 232
657 425 Bin 038 TZT= 232
655 419 Bin 037 TZT= 235
666 420 Bin 036 TZT= 246
672 420 Bin 035 TZT= 252
663 426 Bin 034 TZT= 237
657 427 Bin 033 TZT= 230
663 419 Bin 064 TZT= 244
660 428 Bin 063 TZT= 232
658 428 Bin 062 TZT= 230
660 427 Bin 061 TZT= 232
662 415 Bin 060 TZT= 247
656 414 Bin 059 TZT= 242
657 414 Bin 058 TZT= 243
656 415 Bin 057 TZT= 241
653 423 Bin 056 TZT= 229
657 425 Bin 055 TZT= 232
655 424 Bin 054 TZT= 232
656 425 Bin 053 TZT= 231
655 422 Bin 052 TZT= 233
644 417 Bin 051 TZT= 227
667 419 Bin 050 TZT= 248
674 426 Bin 049 TZT= 248
662 421 Bin 080 TZT= 241
656 423 Bin 079 TZT= 233
656 426 Bin 078 TZT= 230
656 428 Bin 077 TZT= 228
656 418 Bin 076 TZT= 238
658 418 Bin 075 TZT= 240
658 417 Bin 074 TZT= 241
656 419 Bin 073 TZT= 237
647 423 Bin 072 TZT= 224
644 416 Bin 071 TZT= 228
650 425 Bin 070 TZT= 225
651 424 Bin 069 TZT= 228
651 421 Bin 068 TZT= 230
649 421 Bin 067 TZT= 229
656 416 Bin 066 TZT= 240
666 407 Bin 065 TZT= 259
-250 -150
Time Relative to SS (s)

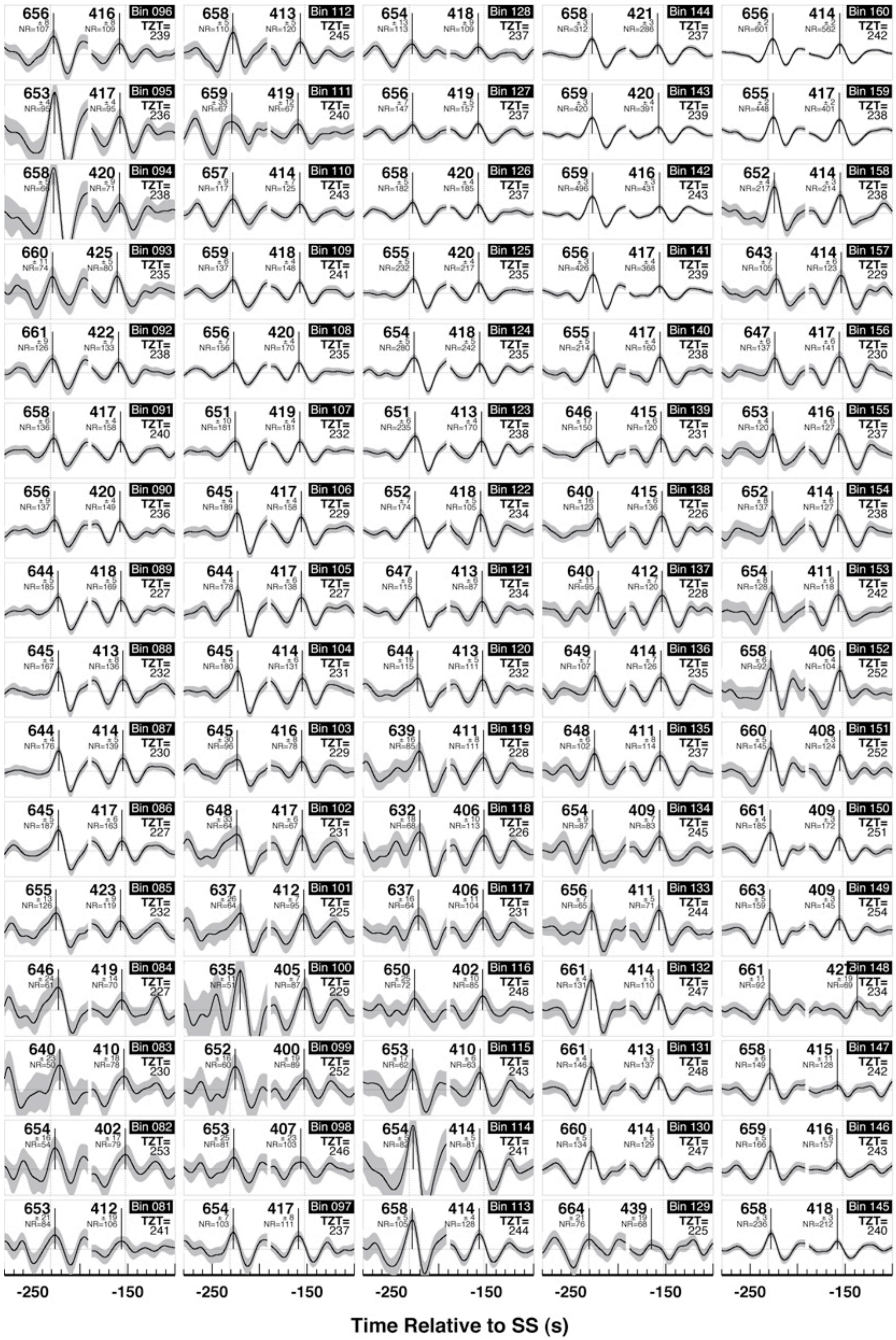
-250
-150
Time Relative to SS (s)

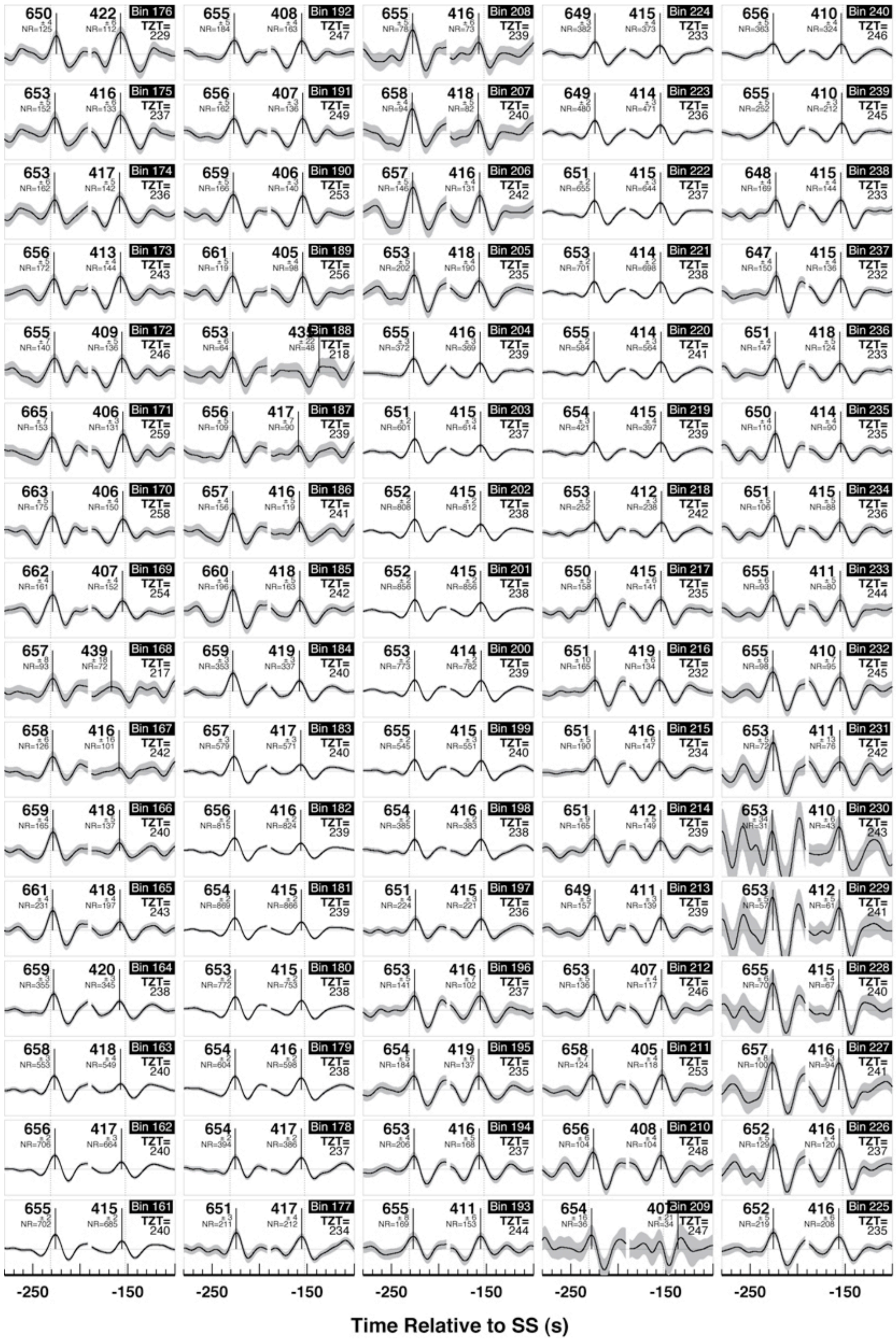
-250
-150
Time Relative to SS (s)

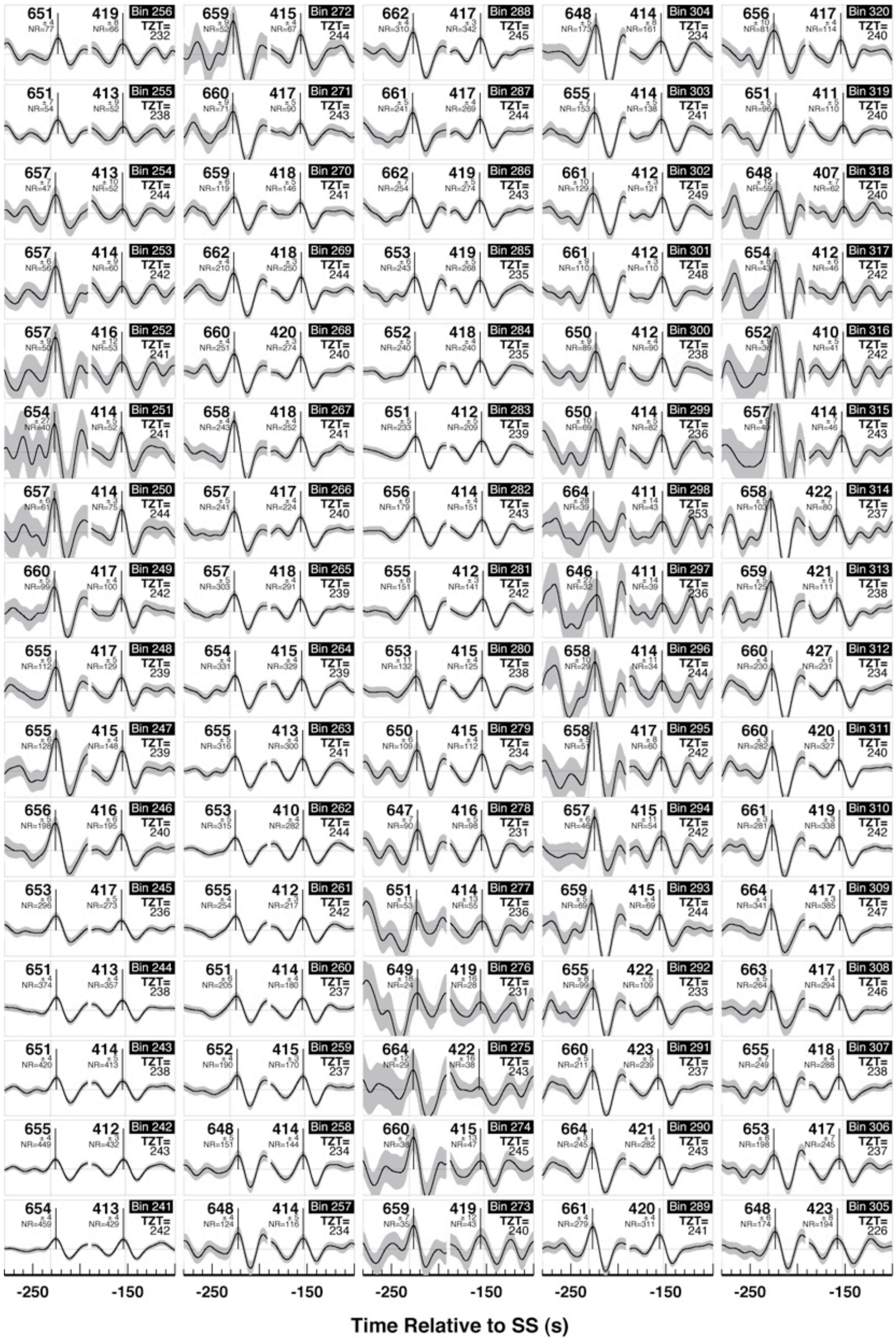
-250
-150
Time Relative to SS (s)

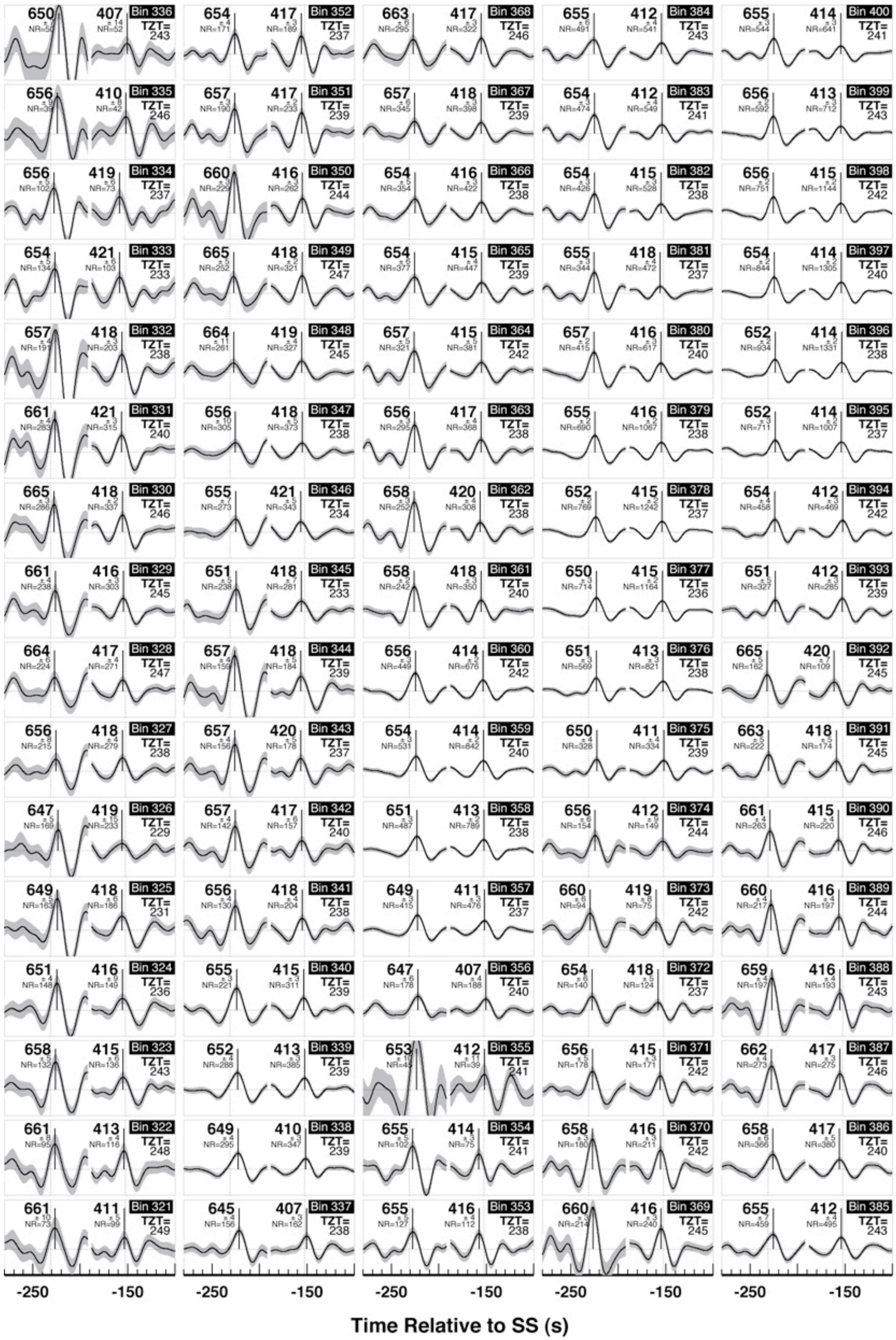
-250
-150
Time Relative to SS (s)

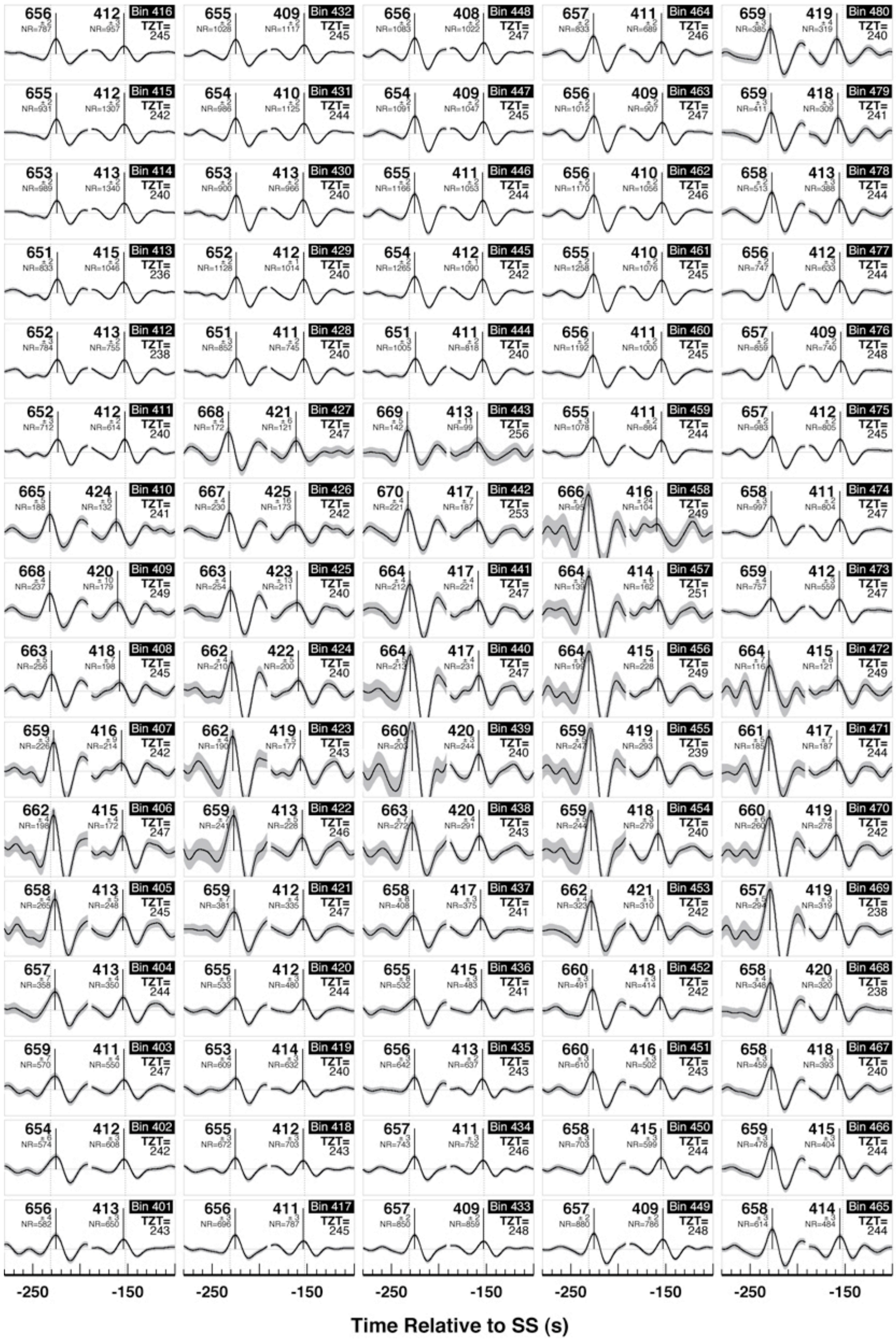

-250
-150
Time Relative to SS (s)

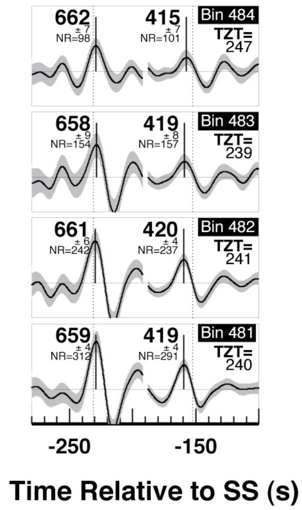

Fig. S2. A catalog of the stacks for our dataset, at a low-pass filter of 15 seconds. The stacks shown are for S670S and S400S. The two different precursor stacks are separated by a small gap at 190 seconds, with a vertical line showing the time pick on each precursory arrival. The narrow dotted line shows the PREM predicted travel times for S670S and S400S. Also shown is the 95% confidence interval computed from 300 random resamplings of the data (gray shading). For each bin we report the modal histogram depth of each boundary, corrected for upper mantle heterogeneity and crustal structure, the histogram standard deviation, and the number of seismic records in each stack. The MTZ thickness measurement (TZT) is reported to the right of the stacks.